

Time resolved optical tomography of the human forearm

Elizabeth M C Hillman¹, Jeremy C Hebden¹, Martin Schweiger¹,
Hamid Dehghani¹, Florian E W Schmidt¹, David T Delpy¹ and
Simon R Arridge²

¹ Department of Medical Physics and Bioengineering, University College London,
11–20 Capper Street, London WC1E 6JA, UK

² Department of Computer Science, University College London, Gower Street,
London WC1E 6BT, UK

Received 25 September 2000

Abstract

A 32-channel time-resolved optical imaging instrument has been developed principally to study functional parameters of the new-born infant brain. As a prelude to studies on infants, the device and image reconstruction methodology have been evaluated on the adult human forearm. Cross-sectional images were generated using time-resolved measurements of transmitted light at two wavelengths. All data were acquired using a fully automated computer-controlled protocol. Images representing the internal scattering and absorbing properties of the arm are presented, as well as images that reveal physiological changes during a simple finger flexion exercise. The results presented in this paper represent the first simultaneous tomographic reconstruction of the internal scattering and absorbing properties of a clinical subject using purely temporal data, with additional co-registered difference images showing repeatable absorption changes at two wavelengths in response to exercise.

1. Introduction

1.1. Optical tomography

Novel optical imaging methods are being developed which aim to exploit the interactions between near infrared (NIR) light and human tissue, and in particular the inherent differences between the absorption spectra of the oxygenated and de-oxygenated forms of haemoglobin, in order to monitor the physiological and metabolic status of living tissue. Researchers in the USA (Benaron *et al* 2000, Grable *et al* 1997, Pogue *et al* 1997, Fantini *et al* 1999, Ntziachristos *et al* 1998, Barbour *et al* 1998), Europe (Kaschke *et al* 1994, Colak *et al* 1997, Grosenick *et al* 1999) and Japan (Eda *et al* 1999, Koizumi *et al* 1999) are developing imaging systems which are currently being evaluated on human subjects. The diffuse nature of NIR light transport in tissues prevents the use of conventional imaging techniques such as the simple transillumination or back-projection methods employed for x-ray imaging. As a result there

are two distinct approaches to NIR imaging. Optical *topography* uses multiple sources and detectors placed on the skin to map changes in the optical properties directly below the surface, or to form a simple projection in a transmittance geometry. Investigators have successfully employed suitable arrays to observe rapid changes in cortical oxygenation in response to specific stimuli such as motor, visual or mental activity (Koizumi *et al* 1999, Franceschini-Fantini *et al* 2000, Chance *et al* 1998). Optical *tomography*, however, involves reconstruction of either a three-dimensional (3D) volume or a transverse slice, sampling deep regions of tissue, and is consequently more difficult. Not only is the collection of data a significant challenge, but sophisticated algorithms are required in order to reconstruct images of the internal optical properties (Pogue *et al* 1997, Colak *et al* 1997, Arridge and Hebden 1997).

A variety of technologies have been explored for acquiring suitable data for optical tomography. The easiest to employ and least expensive to build is a system which records the transmitted intensity at the surface in response to illumination by a continuous source of light. Although measurements of *changes* in intensity have successfully been employed by some researchers (Barbour *et al* 1998, Colak *et al* 1997, Graber *et al* 1993) it is not possible to distinguish between changes in absorption and changes in scatter (Arridge and Lionheart 1998). Furthermore, in the presence of unknown inhomogeneous scattering or absorbing background structure, localization and quantitation of absorption changes may be erroneous (Arridge and Schweiger 1995, Hillman *et al* 2001). Consequently researchers have sought to develop instruments which perform measurements in the time or frequency domain, which provide additional information to allow differentiation between absorbing and scattering structure. In addition, since coupling between the tissue and each source and detector can cause large variations in intensity measurements, and absolute intensity measurements are more strongly influenced by photon interactions at the surface than by regions deep within tissue (Arridge 1995a, b) it is advantageous to use normalized measurements which are independent of absolute intensity. Time domain systems measure the temporal distribution of photons transmitted between two points on the surface in response to illumination by an impulse of light, while frequency domain technology determines the modulation amplitude and phase delay when the source has a continuous, modulated intensity.

The imaging system we have built at University College London (UCL), known as MONSTIR (multi-channel opto-electronic near-infrared system for time-resolved image reconstruction), is based on state-of-the-art time-correlated single photon counting (TCSPC) instrumentation. Its construction and performance specification is described in detail by Schmidt *et al* (2000). It uses microchannel-plate photomultiplier tubes (MCP-PMTs) and fast digital electronics to measure the temporal dispersion of picosecond laser pulses (Ti:sapphire) transmitted through the tissue. A 32-way optical fibre switch allows the light source to be positioned at any of 32 locations, while transmitted light is collected simultaneously by 32 detector fibre bundles. Variable optical attenuators (VOAs) reduce the necessary dynamic range of the detectors by automatically adjusting the intensity of light delivered by each fibre bundle. The raw data measured are histograms of photon flight times called temporal point spread functions (TPSFs).

By extracting *datatypes* from the TPSFs we reduce data redundancy and aid calibration. Datatypes represent various characteristics of the TPSF, e.g. temporal moments (mean flight time, or variance), normalized Laplace and Mellin–Laplace transforms, complex phase and amplitude and integrated intensity (Schweiger and Arridge 1999). Calibration and data extraction techniques depend on the type of reconstruction utilized, as detailed in section 3.

The image reconstruction package we have developed at UCL is known as TOAST (temporal optical absorption and scattering tomography). TOAST employs the finite element method (FEM) to model the propagation of light through tissue using the diffusion

Table 1. Published values for the optical properties of the basic tissue groups of the arm at 800 nm. Taken from Simpson *et al* (1998), Firkbank *et al* (1993), Cheong *et al* (1990) and the spectra in figure 3.

Arm component	μ_a (mm ⁻¹)	μ'_s (mm ⁻¹)
Bone (pig skull)	0.027	1.8
Muscle (exsanguinated abdominal)	0.03	0.7
Blood (arterial) (98%, 2mM l ⁻¹)	0.398	1
Blood (venous) (75%, 2mM l ⁻¹)	0.396	1
Subdermis (human <i>ex vivo</i>)	0.008	1.2

approximation to the radiative transfer equation. Image reconstruction involves iteratively adjusting the optical properties assigned to the FEM mesh to optimize the match of the model to the data (Schweiger *et al* 1993, Arridge and Schweiger 1997). The use of datatypes decreases computation time and the memory requirements of TOAST, which can accommodate combinations of multiple datatypes (Arridge and Schweiger 1993).

1.2. The significance of arm imaging

The ultimate aim of the MONSTIR project is to image the new-born infant brain, where information about absorption and scatter distributions would allow the monitoring of cerebral oxygenation, haemodynamics and variations in myelination and structure. Means of coupling the instrument's optics to the heads of infants are currently being developed and tested. As a prelude to initial tests on infants, MONSTIR has been evaluated on the adult human forearm. In general, a forearm will comfortably conform to a circular cross-section, and therefore coupling the sources and detectors to the skin may be accomplished simply by placing the arm through a plastic circular holder similar to those used previously for phantom studies (Schmidt *et al* 2000, Hebden *et al* 1999). This roughly cylindrical geometry also facilitates 2D and 3D FEM mesh generation and deduction of the spatial co-ordinates of the sources and detectors as required for image reconstruction. The fibre holder ring used here was 7 cm in diameter, which is similar to the dimensions of a 24-week gestation premature infant's head (Johnston 1998, p 45).

Unlike the phantoms used in previous studies, the human forearm is highly heterogeneous, containing bones, muscle, fat and blood vessels, all with optical properties which are known only roughly given the limited data available for *in vivo* and *ex vivo* tissues (Simpson *et al* 1998, Firkbank *et al* 1993, Cheong *et al* 1990). Table 1 shows representative optical properties of each component of the arm. In addition the arm represents a particularly useful target for optical tomography because of the facility it offers to invoke changes in tissue oxygenation and blood flow through appropriate exercise or vessel occlusion.

Figure 1 shows the basic cross-sectional anatomy of the human forearm. The predominant features are the radius and ulna bones. In addition there are a number of arteries of various sizes positioned throughout the arm, together with veins located on the surface of the forearm. The distribution of muscles, their density and optical properties, and also the thickness of the dermis, sub-dermis and fat layer together with the positions and sizes of the blood vessels and bones will depend on the subject's age, sex and arm size.

So far we have explored two methods of reconstructing images from measured data (Hillman *et al* 2000, Arridge *et al* 2000). *Absolute imaging* is where we attempt to use the TOAST reconstruction algorithm to fully model the structure of the arm in terms of its absorption and scatter coefficients. This necessitates an independent method of calibration.

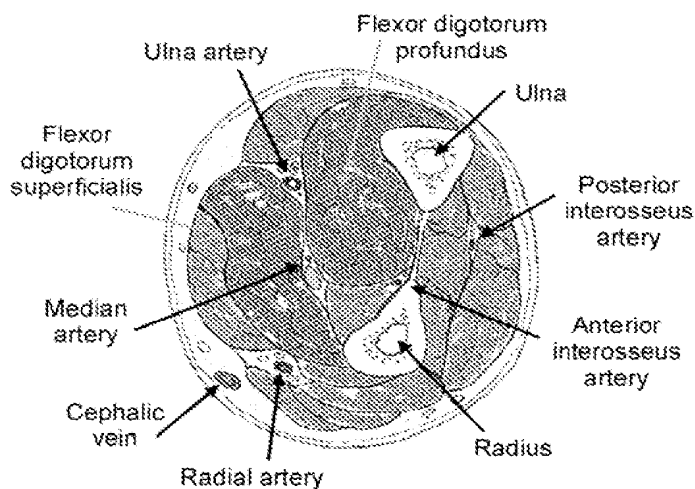


Figure 1. The basic anatomy of the human forearm. The red areas highlight the flexor digitorum profundus and superficialis, since they are the muscles thought to be involved in the simple finger exercises described in section 2.

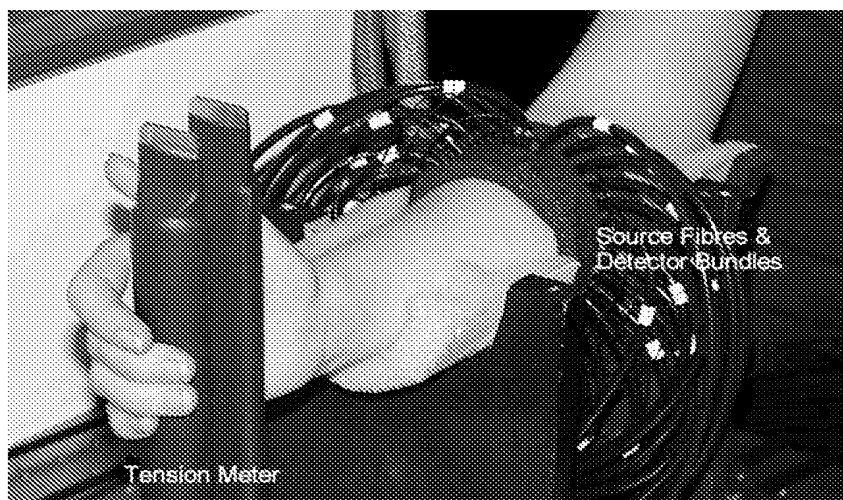


Figure 2. The experimental set-up used to acquire active and resting state time-resolved data on the forearm. Sources fibres and detector fibre bundles are held by the circular black plastic ring, such that the detector bundles are in contact with the skin, while the source fibres are withdrawn by ~ 2 mm. In the image plane, the forearm conforms to the shape of the ring, yielding a circular (7 cm diameter) cross section.

In principle, the two images produced represent the distribution of either scatter or absorption over the cross section of the arm, for whatever state that the arm was in while the image data were acquired.

The other type of imaging that we are able to perform is *difference imaging*. This is a far more common approach to optical tomography that employs two data sets acquired on the

object of interest before and after a change to produce an image revealing only the changes. This means that an independent calibration is no longer required (Hillman *et al* 2000). It is also commonly utilized since if the changes are sufficiently small, it is often assumed that the image reconstruction problem can be linearized. Linearization of the problem means that a sensitivity matrix, or set of PMDFs (photon measurement density functions) (Arridge 1995a, b) relating small changes in the measured parameter to small perturbations in optical properties can be modelled/measured for a given geometry. The changes in optical properties are then directly calculated via linear inversion of *the sensitivity matrix acting on the perturbations in optical properties = changes in measured parameter*. This simple reconstruction method has been shown to produce good images of very simple phantoms with well known reference objects such that changes in measurement can be related to the structure of interest (Eda *et al* 1999, Graber *et al* 1993, O'Leary *et al* 1995). Other researchers have suggested using the average data values as the reference (Ueda *et al* 1997). The TOAST algorithm uses nonlinear methods, but can also be used to deduce the changes in optical properties responsible for changes in measurement. Use of such an iterative nonlinear method effectively allows high contrast highly heterogeneous images to be reconstructed, since it is not limited to the simple assumptions of perturbation theory (Pogue *et al* 1995, Arridge 1999). A problem arises however when data are collected on a heterogeneous object at two different states, such that one data set corresponds to the reference measurement. This reference state will not be well known. This is a major constraint on difference imaging (both linear and nonlinear) since it requires the assumption that it is possible to measure a change occurring within an inhomogeneous medium, and that an image can be produced assuming that this change is equivalent to the same change in a homogeneous/estimated medium. The applicability of this sort of assumption is described in Hillman *et al* (2001) but has yet to be explored in clinical subjects. Its implications are discussed in section 3.2.

We have previously shown that the MONSTIR system can be temporally 'baseline' calibrated to produce absolute images, and the TOAST reconstruction algorithm is capable of producing such images (Hillman *et al* 2000). Since the same systems also have the capacity to explore difference imaging using the same data sets and reconstruction techniques we are able to not only produce difference images, but also co-register them with the absolute background optical properties of the structure as derived from the same data.

In the infant brain monitoring case we are interested in observing changes in the optical properties of regions of the brain. These may be variations in absorption due to changes in blood perfusion/oxygenation (e.g. in hypoxic ischaemia), or changes in the structurally based optical properties of the brain tissue (e.g. degeneration of white matter or *leukomalacia*). The use of multiple wavelengths can provide information about the oxygenation status of the blood in the brain. In addition, baseline information about absolute absorption and scatter can potentially provide useful information about the cerebral anatomy of the infant, and the presence of haematomas or ventricular haemorrhages. These absolute images may also provide valuable *a priori* information to aid better production of subsequent difference images. This would be necessary if the linearization assumptions described above were found to be insufficient for the widely varying optical properties and anatomies encountered in the clinical environment. Corrections might involve using the absolute images to form sensitivity matrices for the heterogeneous structure, allowing a true model of the perturbed image to be created, as has been shown to be effective in simulations (Hillman *et al* 2001). The objective of our arm imaging experiments was then to produce both difference and absolute images simultaneously. Absolute images of scatter should show the bones most prominently, while the absolute absorption images should reveal regional variations in concentrations of the dominant chromophores in the tissues. For difference imaging, a change that is simple to induce is that

resulting from activation of a particular set of muscles through exercise. Although the exact physiological response to the particular exercise that we were able to perform is not known, we are interested in whether we can resolve any changes that correlate with the specific muscle groups that we are attempting to activate. By re-tuning our Ti:sapphire laser, we can repeat our image data acquisitions at different wavelengths. This enables us to produce difference images at multiple wavelengths. The additional information about the wavelength dependence of the absorption changes allows further deductions to be made about the haemodynamic and physiological changes occurring during activation.

2. Experimental method

We performed the arm imaging study on two different volunteers (subjects A and B). Data were acquired by placing a plastic circular fibre holder with diameter 7 cm over the hand and up the forearm until there was good contact between tissue and the ring. The 32 source fibres and 32 detector fibre bundles were positioned alternately and evenly around the ring, in a single plane. The source fibres were withdrawn by 2 mm to reduce coupling variations and the detector bundles were in gentle contact with the skin. Each source sequentially illuminated the opposing 22 detectors for 15 seconds; the VOAs (see section 1.1) were used to de-activate the detectors close to active sources to achieve this fan-beam geometry. We imaged the forearm of subject A on two separate occasions, twice in the second session. Subject B's forearm was imaged once to further verify the results. For each experiment, four sets of imaging data were recorded in rapid succession. First, with the laser tuned to a wavelength of 820 nm, a baseline calibration measurement was performed, followed by a scan with the volunteer's arm remaining stationary in a resting position. The resting position involved the subject lightly holding the tension meter shown in figure 2. During the second scan at the same wavelength, the volunteer gripped the tension meter at around half maximum exertion, between the palm and the index and middle fingers. During a two second delay while the sources and VOAs switched positions, the subject was allowed to briefly loosen the grip, to prevent cramp and fatigue. By avoiding using the thumb or changing the orientation of the wrist during exercise we hope to reduce and localize the number of muscles involved in the exercise. MRI experiments reported by Nelson *et al* (1991) indicate that this exercise activates the flexor digitorum superficialis and the flexor digitorum profundus muscles (see figure 1). Immediately following the 820 nm scans, the laser was re-tuned to 780 nm and another set of data was acquired with the arm at rest, having allowed sufficient time for the arm to return to a rested state. A fourth scan was performed on the exercising arm at the new wavelength, and finally a further baseline calibration measurement was obtained at 780 nm. Figure 3 shows the absorption spectra of oxy- and deoxy-haemoglobin for near infrared wavelengths. The two wavelengths (780 and 820 nm) are located on each side of the isobestic point, at which the characteristic absorption by oxy- and deoxy-haemoglobin are equal, and are hence chosen to highlight differences in signal due to changes in tissue oxygenation. Note that in fact one acquisition was performed at 790 nm due to laser instability. The four data sets and baseline calibrations per subject provide all the data necessary to reconstruct both absolute and difference images, at the two wavelengths.

MRI images of the appropriate plane of the arm of each subject were subsequently collected to provide accurate anatomical information. The MRI images are shown in figure 4: the major anatomical features shown in figure 1 have been identified and the approximate locations of the flexor digitorum superficialis and flexor digitorum profundus have been highlighted. This was done by identifying the MRI plane most similar to figure 1 and then tracing the paths of the muscles up to the level of the fibre holder ring (which was worn by the subject during the MRI to provide the correct circular conformation).

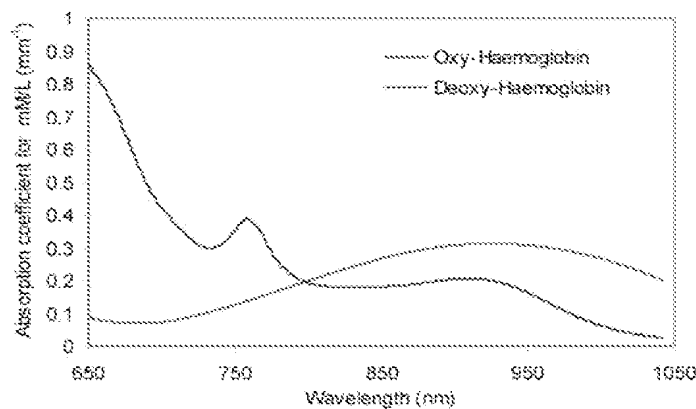


Figure 3. The absorption spectra of oxy- and deoxy-haemoglobin in the near infrared wavelength range. The values shown are the attenuation per millimetre for a 1 mM concentration of haematocrit, measured using a CCD spectrometer.

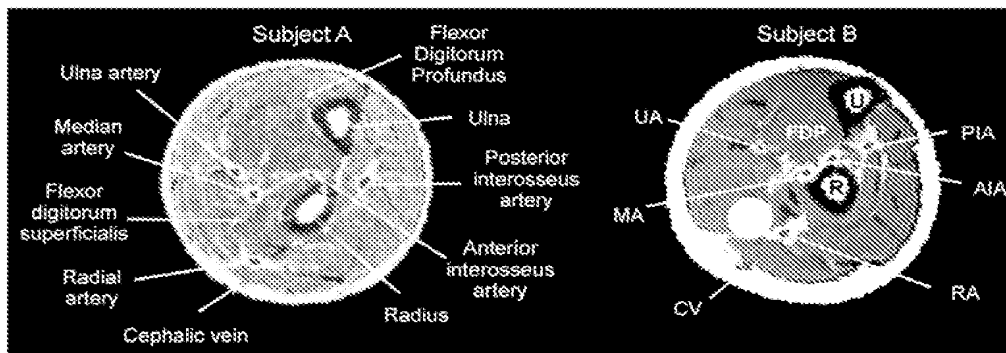


Figure 4. MRI images of the two subjects. The pink regions are the muscle groups thought to be responsible for the exercise performed. The red dots represent arteries.

3. Image production and results

3.1. Absolute images

Full details of the tools used for the baseline measurements can be found in previous publications (Schmidt *et al* 2000, Hillman *et al* 2000). Their use constitutes measuring the impulse response function (IRF) of each source–detector pair. This allows us to correct our measured data for the variability in temporal delay and dispersion due to the different lengths and properties of source fibres, detector bundles, electronic cables and differences between the 32 separate detection systems.

The amount of information required to uniquely and accurately describe a distribution of absorption and scatter has yet to be categorically quantified. Although non-uniqueness of intensity measurements alone has been proven by Arridge and Lionheart (1998), as yet no such result has been produced for mean flight time. We have found using phantoms and simulations that a degree of separation of absorption and scatter for simple structures is possible using just

mean flight time, because the effects of absorption and scatter on the datatype appear to be negatively correlated.

Calibration of our system to account for baseline intensity is not yet possible, and is likely to be problematic in situations where surface coupling of optical fibres is difficult to determine or may vary (as in the case of an infant with hair). The absolute images shown in figure 5 have therefore been produced using only mean flight time data. Calibration was performed by appropriately windowing the measured TPSFs, numerically calculating the mean time and subtracting the meantime of the measured IRF. This is equivalent to de-convolving the IRF from the measured TPSF. The careful windowing enabled the effects of non-convolved features such as stochastic noise and cross-talk to be reduced. Mean time has been found to be a very robust datatype with good sensitivity to both absorbing and scattering structure, with good agreement observed between simulations and measurements of well specified phantoms.

The image reconstruction employed a circular (2D) FEM mesh consisting of 7392 triangular elements. The data had a simple 2D:3D correction applied. Full descriptions of the origin of the correction and the choice of optical properties for calculation of the correction are given in Hillman *et al* (2000). Forward data simulations were performed for a homogeneous cylinder (3D) mesh (consisting of 98 201 second-order elements) and the circular (2D) mesh described above, with optical properties $\mu_a = 0.04 \text{ mm}^{-1}$ and $\mu'_s = 1 \text{ mm}^{-1}$ and the same source-detector geometry as employed in the arm experiments. The 3D simulated values were subtracted from the measured data, and the 2D values were then added. The starting values for the reconstruction were homogeneous $\mu_a = 0.04 \text{ mm}^{-1}$ and $\mu'_s = 1 \text{ mm}^{-1}$. This means that we are assuming that the changes in data corresponding to optical properties differences between the arm and a 3D homogeneous model are the same as those between the 2D arm model derived by TOAST and a 2D homogeneous model. Since the attenuation is high, the corrections are small, as photons do not penetrate far beyond the plane of interest. Qualitatively, application of such a correction to previous phantom and simulated data has been shown to reduce a general ring artefact in μ_a images, and improve the positional accuracy of μ'_s images (Hillman *et al* 2000, Schweiger and Arridge 1998). For clarity, the images shown in figure 5 have been individually scaled linearly between their maximum and minimum values. The colour-map and scale limits for each image are also shown in histogram form on the right (top: μ'_s and bottom: μ_a). The images are all the seventh iteration. TOAST produces both absorption and scatter images simultaneously. Computation of each pair took ~ 30 minutes on a 333 MHz Sun Ultra 5 workstation.

The top set of images shows the results from subject A; the lower set shows the images of subject B. The bones are clearly visible as localized regions of increased scatter. Note that subject B had a smaller arm than subject A, such that the ring was positioned further up the arm where the orientation of the radius and ulna is different. This is supported by the MRI images of both subjects (shown in figure 4). The absolute values found range between 0.6 mm^{-1} and 2 mm^{-1} , indicating good retrieval of the scatter properties of bone and muscle quoted in table 1.

The absolute absorption images do not reveal much high-resolution detail. However, as the MRIs of the arm show, besides the bones, the arm is composed of fairly uniform well packed muscles. There is a regional maximum in absorption towards the centre of the arm, around the area where the arteries are located in both subjects. We can also see there are consistent differences between images collected at 780 nm and 820 nm. For example, for subject A, there is a small region of high absorption at 780 nm at the bottom of the image, but not in the 820 nm images, that may correspond to the cephalic vein. There are also regions of lower absorption corresponding to the bones and the outer skin layer. The range of absorption values is between 0.025 and 0.054 mm^{-1} (note the initial condition was a homogeneous distribution

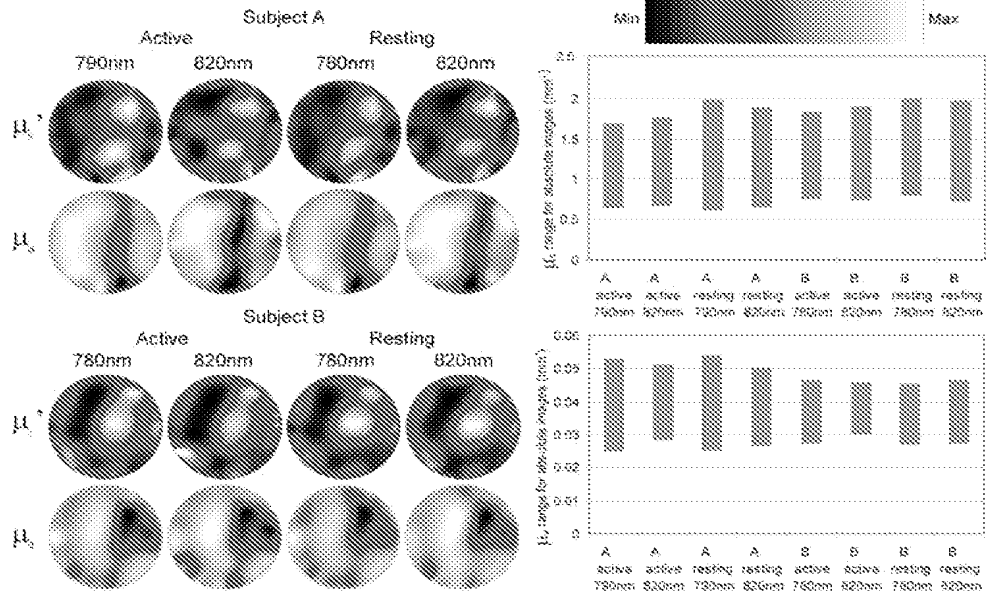


Figure 5. Absolute absorption (μ_a) and scatter (μ_s') images of the forearm at 780 nm/790 nm and 820 nm as described in section 3.1. The images are scaled individually and linearly between their maximum and minimum values. The histograms on the right show the scale ranges for the scatter (top) and absorption (bottom) images.

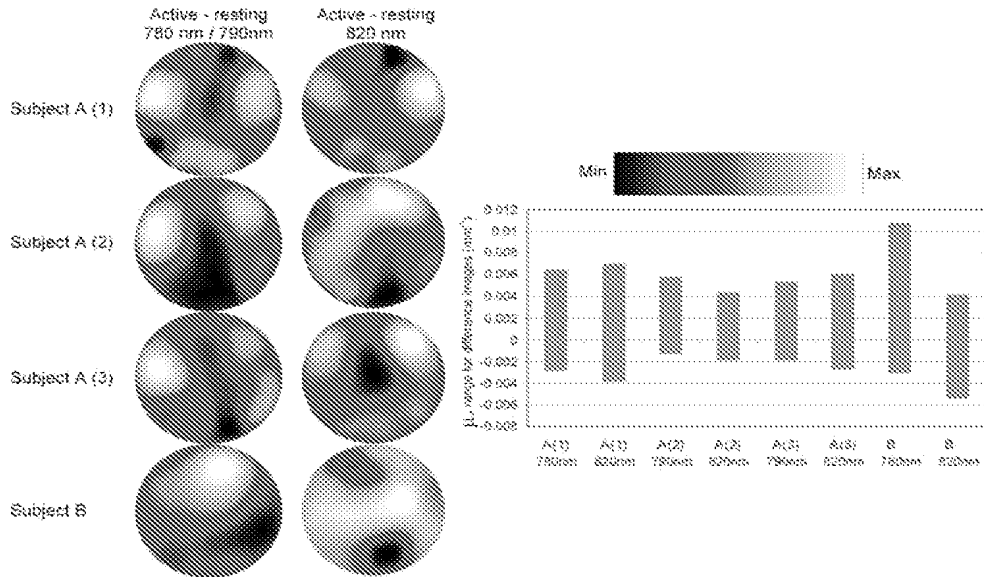


Figure 6. Absorption difference images showing the absorption changes (relative to an initial homogeneous distribution of $\mu_a = 0.04 \text{ mm}^{-1}$) in the forearm during a finger flexure exercise, compared to a resting state at 780 nm/790 nm and 820 nm, as described in section 3.2. The images are scaled individually and linearly between their maximum and minimum values. The histogram on the right shows the scale ranges for each image.

of $\mu_a = 0.04 \text{ mm}^{-1}$, an estimate of the average absorption). Since blood in the muscle will increase the absorption coefficient from that quoted for exsanguinated muscle in table 1, our average absorption for the muscle is reasonable. However given that we cannot expect to have identified the very small arteries as regions of very high ($\sim 0.4 \text{ mm}^{-1}$) absorption the contributions of the arteries will have caused an increase in the average absorption values. Clearly the *relative* absorptions of the various regions; arteries, muscle, bone and dermis, have been identified.

3.2. Difference images

The calibration measurements used to produce the absolute images described in section 3.1 are not required to produce difference images. This is because we are using the differences between the mean times measured in the active and resting states, and also the corresponding ratio of the intensities measured between the two states. Since we are subtracting the mean times of two TPSFs acquired shortly after one another, the IRFs of the system are assumed to have been unchanged, and should thus cancel between the measurements. This is also true of taking the ratio of intensities. In addition, for intensity, surface coupling is a multiplied factor, so if we assume that the coupling is sufficiently stable between the active and resting acquisitions, intensity is available as a datatype for difference imaging (where it was not for absolute imaging).

By only using changes in measurements, TOAST must assume that the differences in the measurements made through the complex structure of the arm are suitably comparable to the changes between a 2D homogeneous model and a 2D model of the changes in absorption. In addition we are assuming that there are no changes in scatter as a result of activation. Thus the difference images shown in figure 6 were reconstructed for absorption *changes* only, at each wavelength on each subject. They were reconstructed on the same 2D mesh as used for the absolute images and have been scaled linearly between their maximum and minimum values. TOAST kept the scatter parameter constant at a value of $\mu'_s = 1 \text{ mm}^{-1}$ (chosen as a approximate value based on the literature; see table 1); the initial μ_a value used was 0.04 mm^{-1} although here we are only interested in changes relative to this value. The images shown correspond to the third iteration of the image reconstructions. The choice of the third iteration here (compared to the seventh for the absolute images) is reasonable considering the magnitude of the changes that we are expecting to see relative to the starting condition. The scales of the absolute images in figure 5 clearly show that the nonlinear algorithm has had to modify the optical properties of the model significantly from the initial homogeneous distribution, compared to the small changes in the difference images indicated by the scales on figure 6. Computation took ~ 4 minutes on a 333 MHz Sun Ultra 5 workstation.

Note that although a 2D mesh was used to reconstruct the difference images, it is not necessary to apply the 2D:3D correction used to produce the absolute images. This is because by using two 3D data sets (the resting and active) to calculate the change in datatype, we are comparing changes in a 3D arm to differences between two 2D models (homogeneous, and the resulting difference image). If we are assuming the same argument as described for the 2D:3D correction given in section 3.1, then the effect of the 3D acquisition geometry should cancel. The robustness of this assumption is discussed further in Hillman *et al* (2001).

We expect to observe differences in the absorption changes at different wavelengths in response to exercise because the wavelengths chosen were either side of 800 nm, which is the isobestic point for the absorption spectra of oxy- and deoxy-haemoglobin (see figure 3). The changes in absorption expected due to either blood volume or blood oxygenation changes are summarized in table 2.

Table 2. The changes in absorption expected in response to increase in oxygenation (SaO_2), and increase in blood volume (HbVol) at <800 nm and >800 nm.

	<800 nm μ_a	>800 nm μ_a
$\text{SaO}_2 \uparrow$	\downarrow	\uparrow
HbVol \uparrow	\uparrow	\uparrow

The three sets of images for subject A all show similar changes in the absorption at the wavelength used, 780 nm or 820 nm, in response to the exercise performed. At 780 nm an increase in absorption is seen on the left of the image, corresponding to the region containing the flexor muscles (see figure 4). A smaller increase in absorption is also seen on the right side of the image. This may correspond to an area around the posterior interosseus artery or perhaps an extensor muscle, or a muscle that maintains the position of the wrist. In the 820 nm images we see very similar patterns in absorption although in these images it is the area on the right of the images that shows the most significant absorption increase, with the area on the left showing a smaller absorption increase. This consistent pattern, and differing magnitude of the changes in the same regions at different wavelengths supports the premise that the changes that we are seeing are genuine responses to activation. For example, if the change were due to an optode coupling difference occurring during exercise, we would see the same changes in the 820 and 780 nm images. By examining table 2 we can propose then that the absorption changes seen on the left in subject A correspond to an increase in blood volume, with a decrease in oxygenation of the flexor muscles during activation. On the right, we may be seeing an increase in oxygenation and an increase in blood volume near the posterior interosseous artery, or a wrist or extensor muscle, which could suggest that the area is less well perfused in the resting position, or that further muscles are also involved in the exercise.

In subject B we see an increase in absorption in the 780 nm image that corresponds well to the region identified as the flexor digitorum profundus in the MRI image. In the 820 nm image we do not see an increase in the same region, but we see an increase in the centre of the arm which may correspond to the subject's apparent concentration of arteries along this line as shown in the MRI. Again by examining table 2 we see that these results for subject B suggest a regional decrease in oxygenation in the flexor region during activation, coupled with an increase in oxygenation around the arteries.

These results suggest that in this fairly simple case we have seen physiologically reasonable, and repeatable changes in absorption in response to muscle activation. Note however that these difference images will, to some degree, have been affected by the assumptions mentioned in section 1.2, notably the applicability of linearization of the problem without prior knowledge of the absolute parameters. Simulations have shown that the applicability of the perturbation approach to increasingly complex structures may introduce both quantitative and positional errors in localizing absorption changes where only the differences in measurements are used (Hillman *et al* 2001). Development is now continuing to include more *a priori* information about the background absorption and scatter properties of the object being imaged to try to overcome the limitations of the simple linearization approach. Furthermore, a full 3D reconstruction of both the absolute and difference images would obviate the need for a 2D:3D correction.

Note that we only compute images for data collected at each wavelength, and avoid reconstruction of images that reflect the changes between measurements made at different wavelengths. We believe that development of both background absorption *and* scatter priors will be necessary if *wavelength difference* imaging is to be successful. If the measuring

instrument's systematic errors are wavelength invariant the perturbation approximations will still break down if the initial absorption distribution is not known. Correction for such subtle effects will be required to produce images where wavelength information can be truly combined to provide clear images of oxygen saturation.

4. Discussion

The human arm has been a convenient and popular recent target for groups investigating optical tomography techniques, as it was during the initial stages of development of electrical impedance tomography (EIT) (Barber and Brown 1984) and microwave tomography (Jofre *et al* 1990). Probably the first cross-sectional image of the arm obtained optically was that generated by a research group at Keele University (UK), who employed simple intensity measurements and an algorithm previously developed for EIT (Wickramasinghe 1994). The first attempt at functional imaging of the forearm using optical techniques was published by Maris *et al* (1994), who employed a frequency domain system to map *topographic* differences in the haemoglobin oxygenation in finger extensor muscles during exercise. These were generated from measurements of the reflected light on the surface of the arm using a fixed source–detector separation of 31 mm. Data analysis consisted of a simple subtraction of the average phase measurement during rest from the average phase measurement during muscle contraction. Barbour *et al* (1998) later employed a continuous wave (CW) system to obtain cross-sectional images of muscle activation in the forearm using only differences in intensity measurements and a linearized perturbation-based iterative back-projection algorithm. Measurements were also obtained with and without a pressure cuff inflated on the upper arm to impede blood flow in the forearm. More recently, the same group have reported results of further series of arm imaging experiments with fast, and repeated acquisitions of intensity changes. The results then use the time-series information about the activity in an attempt to identify the flexor and extensor muscles responsible for the repeated movement of the fourth digit, the real-time response to occlusion produced by a pressure cuff, and the response of the vasculature to contralateral cold shock (Graber *et al* 2000, Blattman *et al* 2000, Barbour *et al* 2000). These methods assume that only changes in absorption are occurring (since the intensity change measurements will not be able to distinguish between absorption and scatter changes (Arridge and Lionheart 1998). In addition, the difficulty of baseline calibration and the lack of temporal information in a CW instrument means that no attempt can be made to derive images of the absolute background structure of the arm (e.g. bones).

Another demonstration of the use of NIR measurements to image the exercising forearm has been recently described by Arakaki *et al* (2000). A time-domain system was employed to acquire a series of TPSFs between sources and detectors positioned in separate rings around the forearm. Estimates of the changes in tissue absorption in response to finger flexion exercise at two wavelengths (780 nm and 830 nm) were used to reconstruct a cross-sectional image representing haemoglobin concentration. Unfortunately the system's signal to noise and dynamic range did not facilitate measurement at large source-detector separations, and consequently the image demonstrates no sensitivity to structure near the centre of the arm. Furthermore, the reconstruction method required immersion of the arm in an intralipid (Choukeife and L'Huillier 1999) matching fluid, which would not be appropriate for imaging of the neonatal brain.

We have presented results showing repeatable changes in absorption in the arm in response to exercise at two wavelengths. In a second subject the 'activation' signal is different but also indicates physiologically reasonable changes in response to exercise. In addition, the same data have yielded multiple and repeatable absolute images of absorption and scatter that

correspond very well with MRI scans of the two subjects. These have allowed the orientation of the absorption changes to be correlated to the position of the bones.

This work has been performed as a step towards development of a functional imaging system for the neonatal brain. Our ability to obtain consistent results and also derive information about absolute structures that correspond well to MRI is encouraging. The difference images shown have provided consistent and repeatable illustrations of the arm's physiological response to exercise.

Acknowledgments

Further information about this work and the availability of our software, data and phantoms can be obtained from the website of the UCL biomedical optics research group (www.medphys.ucl.ac.uk/research/borg). We gratefully acknowledge the support for this research provided by the Wellcome Trust.

References

- Arakaki L S L, Ntziachristos V, Chance B, Leigh J S and Schotland J S 2000 Optical diffusion tomography of the exercising human forearm *Biomedical Topical Meetings, OSA Tech. Digest (Washington, DC, 2000)* pp 374–7.
- Arridge S R 1995a Photon measurement density functions. Part 1: Analytical forms *Appl. Opt.* **34** 7395–409
- 1995b Photon measurement density functions. Part 2: Finite element calculations *Appl. Opt.* **34** 8026–37
- 1999 Optical tomography in medical imaging *Inverse Problems* **15** 41–93
- Arridge S R and Hebden J C 1997 Optical imaging in medicine: modelling and reconstruction *Phys. Med. Biol.* **42** 841–53
- Arridge S R, Hebden J C, Schweiger M, Schmidt F E W, Fry M E, Hillman E M C, Dehghani H and Delpy D T 2000 A method for 3D time-resolved optical tomography *Int. J. Imaging Syst. Tech.* **11** 2–11
- Arridge S R and Lionheart W R B 1998 Nonuniqueness in diffusion-based optical tomography *Opt. Lett.* **23** 882–4
- Arridge S R and Schweiger M 1993 The use of multiple data-types in time-resolved optical absorption and scattering tomography *Proc. SPIE* **2035** 218–29
- 1995 Sensitivity to prior knowledge in optical tomographic reconstruction *Proc. SPIE* **2389** 378–88
- 1997 Image reconstruction in optical tomography *Phil. Trans. R. Soc. B* **352** 717–26
- Barber D C and Brown B H 1984 Applied potential tomography *J. Phys. E: Sci. Instrum.* **17** 723–32
- Barbour R L, Andronica R, Sha Q, Graber H L and Soller I 1998 Development and evaluation of the IRIS-OPTI scanner, a general-purpose optical tomographic imaging system *OSA TOPS* **21** 251–5
- Barbour R L, Graber H L, Zhong S, Pei Y, Hira J and Arif I 2000 Optical imaging of the response of vascular dynamics to a cold shock *Biomedical Topical Meetings, OSA Tech. Digest (Washington, DC, 2000)* pp 430–2
- Benaron D A, Hintz S R, Villringer A, Boas D, Kleinschmidt A, Frahm J, Hirth C, Obrig H, van Houten J C, Kermit E L, Cheong W and Stevenson D K 2000 Noninvasive functional imaging of human brain using light *J. Cereb. Blood Flow Metab.* **20** 469–77
- Blattman S, Graber H L, Zhong S, Pei Y, Arif I, Hira J and Barbour R L 2000 Imaging of tissue reperfusion by dynamic optical tomography *Biomedical Topical Meetings, OSA Tech. Digest (Washington, DC, 2000)* pp 409–10
- Chance B, Anday E, Nioka S, Zhou S, Hong L, Worden K, Li C, Murray T, Ovetsky Y, Pidikiti D and Thomas R 1998 A novel method for fast imaging of brain function non-invasively with light *Opt. Express* **2** 411–23
- Cheong W, Pahl S A and Welch A J 1990 A review of the optical properties of biological tissues *IEEE. J. Quantum Electron.* **26** 2166–85
- Choukeife J E and L'Huillier J P 1999 Measurements of scattering effects within tissue-like media at two wavelengths of 632.8 nm and 680 nm *Lasers Med. Sci.* **14** 286–96
- Colak S B, Papaioannou D G, 't Hooft G W, van der Mark M B, Schomberg H, Paasschens J C J, Melissen J B M and van Asten N 1997 Tomographic image reconstruction from optical projections in light-diffusing media *Appl. Opt.* **36** 180–213
- Eda H, Oda I, Ito Y, Wada Y, Oikawa Y, Tsunazawa Y, Tsuchiya Y, Yamashita Y, Oda M, Sassaroli A, Yamada Y and Tamura M 1999 Multichannel time-resolved optical tomographic imaging system *Rev. Sci. Instrum.* **70** 3595–602
- Fantini S, Franceschini M A, Gratton E, Hueber D, Rosenfeld W, Maulik D, Stubblefield P G and Stankovic M R 1999 Non-invasive optical mapping of the piglet in real time *Opt. Express* **4** 308–14

- Firbank M, Hiraoka M, Essenpreis M and Delpy D T 1993 Measurement of the optical properties of the skull in the wavelength range 650–950 nm *Phys. Med. Biol.* **38** 503–10
- Franceschini-Fantini M A, Toronov V, Filiaci V, Gratton E and Fantini S 2000 On-line optical imaging of the human brain with 160-ms temporal resolution *Opt. Express* **6** 49–57
- Graber H L, Chang J, Lubowsky J, Aronson R and Barbour R L 1993 Near infrared absorption imaging of dense scattering media by steady-state diffusion tomography *Proc. SPIE* **1888** 372–86
- Graber H L, Zhong S, Pei Y, Arif I, Hira J and Barbour R L 2000 Dynamic imaging of muscle activity by optical tomography *Biomedical Topical Meetings, OSA Techn. Digest (Washington, DC, 2000)* pp 407–8
- Grable R J, Rohler D P and Sastry K L A 1997 Optical tomography breast imaging *Proc. SPIE* **2979** 197–210
- Grosenick D, Wabnitz H, Rinneberg H H, Moesta T and Schlag P M 1999 Development of a time-domain optical mammography and first *in vivo* applications *Appl. Opt.* **38** 2927–43
- Hebden J C, Schmidt F E W, Fry M, Schweiger M, Hillman E M C, Delpy D T and Arridge S R 1999 Simultaneous reconstruction of absorption and scattering images by multichannel measurement of purely temporal data *Opt. Lett.* **24** 534–6
- Hillman E M C, Dehghani H, Hebden J C, Arridge S R, Schweiger M and Delpy D T 2001 Differential imaging in heterogeneous media: limitations of linearization assumptions in optical tomography *Proc. SPIE* **4250** at press
- Hillman E M C, Hebden J C, Schmidt F E W, Arridge S R, Schweiger M, Dehghani H and Delpy D T 2000 Calibration techniques and datatype extraction for time-resolved optical tomography *Rev. Sci. Instrum.* **71** 3415–27
- Jofre L, Hawley M S, Broquetas A, de los Reyes E, Ferrando M and Elias-Fusté A R 1990 Medical imaging with a microwave tomographic scanner *IEEE Trans. Biomed. Eng.* **37** 303–12
- Johnston P G B 1998 *The Newborn Child* 8th edn (Churchill Livingstone)
- Kaschke M, Jess H, Gaida G, Kaltenbach J and Wrobel W 1994 Transillumination imaging of tissue by phase modulation techniques *OSA Proc.* **21** 88–92
- Koizumi H, Yamashita Y, Maki A, Yamamoto T, Ito Y, Itagaki H and Kennan R 1999 Higher-order brain function analysis by trans-cranial dynamic near-infrared spectroscopy imaging *J. Biomed. Opt.* **4** 403–13
- Maris M, Gratton E, Maier J, Mantulin W and Chance B 1994 Functional near-infrared imaging of deoxygenated hemoglobin during exercise of the finger extensor muscles using the frequency-domain technique *Bioimaging* **2** 174–83
- Nelson S J, Taylor J S, Vigneron D B, Murphy-Boesch J and Brown T R 1991 Metabolite images of the human arm: changes in spatial and temporal distribution of high energy phosphates during exercise *NMR Biomed.* **4** 268–73
- Ntziachristos V, Ma X and Chance B 1998 Time-correlated single photon counting imager for simultaneous magnetic resonance and near-infrared mammography *Rev. Sci. Instrum.* **69** 4221–33
- O’Leary M A, Boas D A, Chance B and Yodh A G 1995 Experimental images of heterogeneous turbid media by frequency-domain diffusing-photon tomography *Opt. Lett.* **20** 426–8
- Pogue B W, Patterson M S, Jiang H and Paulsen K D 1995 Initial assessment of a simple system for frequency domain diffuse optical tomography *Phys. Med. Biol.* **40** 1709–29
- Pogue B W, Testorf M, McBride T, Osterberg U and Paulsen K 1997 Instrumentation and design of a frequency-domain diffuse optical tomography imager for breast cancer detection *Opt. Express* **1** 391–403
- Schmidt F E W, Fry M E, Hillman E M C, Hebden J C and Delpy D T 2000 A 32-channel time-resolved instrument for medical optical tomography *Rev. Sci. Instrum.* **71** 256–65
- Schweiger M and Arridge S R 1998 Comparison of two- and three-dimensional reconstruction methods in optical tomography *Appl. Opt.* **37** 7419–28
- 1999 Application of temporal filters to time resolved data in optical tomography *Phys. Med. Biol.* **44** 1699–717
- Schweiger M, Arridge S R and Delpy D T 1993 Application of the finite-element method for the forward and inverse models in optical tomography *J. Math. Imaging Vision* **3** 263–83
- Simpson C R, Kohl M, Essenpreis M and Cope M 1998 Near infrared optical properties of *ex vivo* human skin and sub-cutaneous tissues measured using the Monte Carlo inversion technique *Phys. Med. Biol.* **43** 2465–78
- Ueda Y, Ohta K, Oda M, Miwa M, Yamashita Y and Tsuchiya Y 1997 Optical imaging reconstruction using the average value as the reference *Proc. SPIE* **2979** 795–806
- Wickramasinghe Y 1994 *1st EC-BIOMED Workshop in NIR Imaging in Medicine (Bad Wörishofen, 1994)*